Journal of Advanced Joining Processes 14 (2026) 100414

Contents lists available at ScienceDirect

Journal of Advanced Joining Processes

journal homepage: www.sciencedirect.com/journal/journal-of-advanced-joining-processes

# Achieving high productivity in wire-arc directed energy deposition of magnesium alloy thin-walled structures via active cooling

Hyu Kudo [a], Houichi Kitano [b], Hiroyuki Sasahara [c], Hideaki Nagamatsu [a,*]

[a] Department of Mechanical Engineering and Intelligent Systems, The University of Electro-Communications 1-5-1 Chofugaoka, Chofu-shi, Tokyo 182-8585, Japan
[b] National Institute for Materials Science, Research Center for Structural Materials 1-2-1 Sengen, Tsukuba, Ibaraki 305-0047, Japan
[c] Department of Mechanical Systems Engineering, Tokyo University of Agriculture and Technology 2-24-16 Naka-cho, Koganei City, Tokyo 184-8588, Japan

ARTICLE INFO

*Keywords:*
Wire-arc directed energy deposition
Manufacturing rate
Magnesium alloy
Microstructure
Tensile properties
Fractography
Smut

ABSTRACT

Wire-arc directed energy deposition (DED) with high heat input typically requires long inter-pass intervals to avoid deteriorating metallurgical and mechanical properties. However, this significantly extends process time, thereby sacrificing the manufacturing rate (MR). This trade-off is particularly pronounced in thin-walled structures due to low heat dissipation. While solid-contact active cooling (SCAC) can improve the metallurgical and mechanical properties of magnesium alloys in wire-arc DED, its potential for aggressive MR enhancement remains under-explored. This study experimentally reveals that SCAC enables the fabrication of AZ31 thin walls with a refined microstructure and acceptable tensile properties even under a very short interval (average 2.5 s) corresponding to an extremely high MR (882 $cm^3$/h). While natural cooling (NC) exhibited continuous heat accumulation leading to bead sagging despite a 120 s interval (MR = 90 $cm^3$/h), SCAC reached thermal equilibrium early, enabling nearly continuous deposition. Additionally, narrowing the gap between the cooling copper blocks reduced the molten pool volume. Furthermore, the refinement of grains and precipitates by SCAC promoted a transition from a predominant quasi-cleavage mode to an extensive ductile fracture mode. Consequently, SCAC increased the yield strength, tensile strength, and elongation by up to 12 MPa, 13 MPa, and 10%, respectively, along the travel direction. Microstructural analysis suggests that the yield strength enhancement is primarily governed by grain refinement. This work demonstrates that active cooling strategies, including but not limited to SCAC or magnesium alloys, possess the potential to maintain the overall mechanical properties while significantly enhancing productivity in wire-arc DED.

## Introduction

Magnesium (Mg) alloys are widely used in the automotive and aerospace industries due to their light weight and high specific strength (Tan and Ramakrishna, 2021). Accordingly, the application of additive manufacturing (AM) to Mg alloys is being explored for advanced product development. Current studies focus on powder bed fusion (PBF) (Ladani and Sadeghilaridjani, 2021) and directed energy deposition (DED) (Wang et al., 2020). Among DED processes, wire-arc DED offers several advantages, including low cost, high deposition rates (DR), and suitability for large-scale fabrication (Oliveira et al., 2022; Rodrigues et al., 2019). Here, DR is defined as the material volume supplied per unit time. Furthermore, wire-arc DED avoids issues related to the flammability and low laser absorptivity of Mg alloys because it uses arc discharge for melting (Al-Kazzaz et al., 2008; Guo et al., 2016).

However, the high heat input of wire-arc DED causes significant heat accumulation in the deposited layers and the substrate. The resulting high temperatures and rapid thermal cycles not only deteriorate geometric accuracy due to bead sagging but also affect the microstructure (Kamado et al., 1987). Since Mg alloys are particularly sensitive to grain size regarding mechanical properties (Yang et al., 2024), this heat accumulation leads to grain coarsening, consequently reducing both

*Abbreviations:* Mg, Magnesium; AM, Additive manufacturing; PBF, Powder bed fusion; DED, Directed energy deposition; DR, Deposition rate; MR, Manufacturing rate; AC, Active cooling; SCAC, Solid-contact active cooling; NC, Natural cooling; SEM, Scanning electron microscope; TEM, Transmission electron microscopy; EDS, Energy-dispersive spectroscopy; CMT, Cold metal transfer; DC, Directed current; EDM, Electrical discharge machining; HAZ, Heat-affected zone; FZ, Fusion zone; G, Temperature gradient; R, Solidification rate; YS, Yield strength; UTS, Ultimate tensile strength; EL, Elongation.

* Corresponding author.
*E-mail address:* H.nagamatsu@uec.ac.jp (H. Nagamatsu).

https://doi.org/10.1016/j.jajp.2026.100414

Available online 16 June 2026

strength and ductility (Ma et al., 2023). Common countermeasures include reducing heat input or introducing inter-pass intervals (Lei et al., 2018; Wang et al., 2021). Ma et al. (2023) reported that intervals of 60 s or more can improve the geometric accuracy and tensile properties in the wire-arc DED of AZ31 Mg alloy. However, such long intervals significantly extend the process time, thereby reducing the manufacturing rate (MR). Here, MR is defined as the effective volume of material deposited per unit of total process time.

Fig. 1 shows the relationship between DR and MR in wire-arc DED, with a particular focus on Mg alloys. The dashed line represents MR = DR; data points closer to this line indicate shorter intervals. Note that not all referenced studies aimed to maximize MR. Additionally, since steel has a higher density than light metals, its volume-based DR tends to be lower. The DR ($cm^3$/h) and MR ($cm^3$/h) are calculated as follows:

$$\mathrm{DR} = \pi(\varnothing/2)^2 \times \mathrm{WFS} \times 600 \tag{1}$$

$$\mathrm{MR} = \mathrm{DR} \times L/(L + \mathrm{TS} \times T_{\mathrm{dwell}}) \tag{2}$$

where $\varnothing$ (mm) is the wire diameter, $L$ (mm) is the bead length per layer, TS (mm/min) is the travel speed, WFS (m/min) is the wire feed speed, $T_{\mathrm{dwell}}$ (min) is the inter-pass interval. The cases in Fig. 1 and the derivation processes are summarized in Table A.1. Notably, in many previous studies, MR decreases to less than 30% of DR. Relatively high MR and DR have been reported by Zhao et al., Wang et al., and WAAM3D Limited. Zhao et al. (2020) optimized fabrication parameters to produce a large aluminum alloy structure with a diameter of 1000 mm and a height of 550 mm. This process achieved an estimated MR of 317 $cm^3$/h without interrupting the arc. Wang et al. (2023) developed a double-wire process to fabricate a large-scale steel structure, attaining a total mass exceeding 200 kg with a high DR of 1282 $cm^3$/h. Similarly, WAAM3D Limited (2021) fabricated a large steel structure using the same process, achieving an MR of 5 kg/h, which corresponds to 637 $cm^3$/h. In such large-scale fabrications, the heat capacity is large and the long return time to the same deposition point allows sufficient heat dissipation, shortening required intervals. In contrast, when fabricating medium-to-small thin-walled structures, distortion and geometric irregularities occur more easily. For instance, Wang et al. (2023) fabricated a thin-walled steel structure (220 mm × 120 mm × t 2.35 mm) using a high DR of 1154 $cm^3$/h. However, as a 7-minute inter-pass interval was required for thermal management, the MR decreased significantly to 39 $cm^3$/h. Consequently, the reduction in MR due to thermal management requirements remains a critical challenge for thin-walled fabrication (Casuso et al., 2021; Teixeira et al., 2023).

To simultaneously improve MR and the quality of a fabricated component, active cooling (AC) has attracted attention. Direct water cooling is highly effective, enabling high-speed fabrication while maintaining tensile properties of aluminum alloys (Da Silva et al., 2020) and stainless steel (Jorge et al., 2025). However, direct water cooling is unsuitable for Mg alloys due to the risk of combustion and hydrogen-induced porosity. Therefore, we focused on solid-contact active cooling (SCAC), where a high-thermal-conductivity material, such as pure copper, directly contacts the deposited metal. Li et al. (2024) improved the strength and elongation of a WE43 Mg alloy thin wall by placing water-cooled plates near the thin wall for indirect cooling. Ma et al. (2025) reported that SCAC using water-cooled copper blocks successfully shortened intervals and enhanced the tensile properties of an AZ31 thin wall. While current applications are limited to wall structures, SCAC possesses the potential for expansion into free-form fabrication by evolving from plate-based media to roller-based cooling systems. For instance, although not intended for AC, Xie et al. (2016) successfully manufactured meter-sized turbine blades by rolling the sides of the bead with two rollers.

As shown in Fig. 1, the MR of AC (blue circles) is higher than that of natural cooling (NC, blue triangles); however, the maximum reported value is only 364 $cm^3$/h (Da Silva et al., 2020), with no reports of significant further improvements. Furthermore, while the studies by Li et al. (2024) and Ma et al. (2025) provide important insights into the effects of SCAC on metallurgical and mechanical properties, their studies focused on consistent intervals or inter-pass temperatures. Consequently, their assessments are limited to conditions where advantages of SCAC are inherent.

The objective of this study is to clarify the effectiveness of SCAC under high-MR conditions involving high DRs and short inter-pass intervals. To this end, thin-walled structures, which are highly susceptible to heat accumulation, were fabricated using both NC and SCAC at a high DR (1086 $cm^3$/h). The average intervals for NC and SCAC were approximately 120 s and 2.5 s, respectively; the latter corresponding to MR of 882 $cm^3$/h. Thermal histories were recorded using thermocouples, while grain size and secondary phase particles were characterized via optical microscopy, a scanning electron microscope (SEM), and

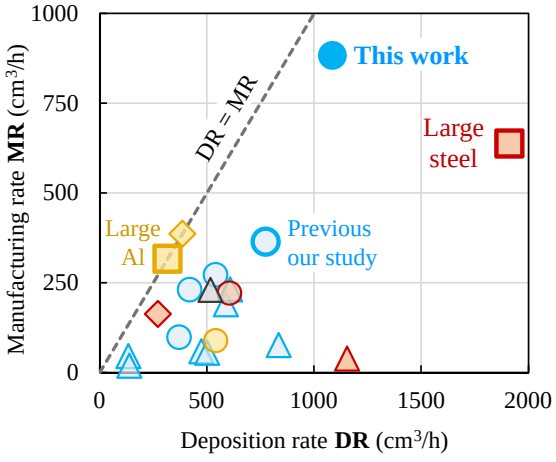


| Color | Material |
|---|---|
| Blue | Magnesium alloy |
| Yellow | Aluminum alloy |
| Red | Steel |
| Gray | Titanium alloy |

| Marker | Scale/shape | Cooling |
|---|---|---|
| ○ Circle | Thin wall | SCAC |
| ◇ Rhombus | Thin wall | AC excluding SCAC |
| △ Triangle | Thin wall | NC |
| □ Square | Large | NC |

**Fig. 1.** Comparisons of manufacturing rates for wire-arc DED components.

energy-dispersive spectroscopy (EDS). Furthermore, the mechanical performance was evaluated through tensile testing and fractographic analysis. This work demonstrates that active cooling strategies, including but not limited to SCAC or magnesium alloys, possess the potential to maintain the overall mechanical properties while significantly enhancing productivity in wire-arc DED.

## Experimental methodology

### *Material used*

Table 1 presents the nominal chemical compositions of the filler wire and the substrate used equivalent to AZ31 Mg alloy. The wire diameter is 1.2 mm, and the substrate dimensions are 150 mm × 40 mm × 10 mm. Table 2 lists the physical properties of the copper block employed as the cooling medium, which conform to the JIS C1100P standard.

### *Fabrication process*

Fig. 2 shows a schematic of the SCAC system. The wire-arc DED setup consists of a six-axis robot (KR 10 R1100 sixx, KUKA AG) and a cold metal transfer (CMT) welder (TPS 500i, Fronius International GmbH). Stringer beads with a path length of 90 mm were deposited in the gap between two parallel copper blocks (Fig. 2a). The torch travel direction was reversed after each layer to ensure structural symmetry. In the AC process, the continuous fabrication of four layers and a 10 s arc-stop were repeated. During these continuous fabrications, the torch was adjusted along the Z-axis to keep the torch-to-work distance within the range of 16.2–22.0 mm. During the arc-stop period, the copper blocks were elevated by the height corresponding to four layers (Fig. 2b). This cycle was repeated until the total build height reached approximately 80 mm. Throughout the fabrication, no bonding occurred between the molten Mg and the copper blocks.

The copper blocks, measuring 200 mm × 22 mm × 22 mm, incorporate an internal channel with a diameter of 14.5 mm. These blocks are connected to a cooling water circulator (PU701, DAIHEN Corp.) via fittings and hoses. Cooling water, with an initial temperature of approximately 25 °C, was constantly circulated through the copper blocks at a flow rate of 13 L/min and a velocity of 1.3 m/s.

Table 3 lists the fabrication conditions for the three thin-walled structures investigated in this study: NC, AC-W11, and AC-W8. AC-W11 and AC-W8 denote walls fabricated using SCAC with copper block gaps ($W$) of 11.3 mm and 8.2 mm, respectively. The fabrication parameters were consistent across all three conditions, except for the cooling method, inter-pass interval $T_{dwell}$, $W$, and the number of layers. A direct current (DC) pulsed mode was employed, with argon gas (≥ 99.99% purity) used as the shielding gas. The torch path length per layer was 90 mm, resulting in a bead length of 95 mm. For AC-W11 and AC-W8, the average layer heights were approximately 2.8 mm and 3.8 mm, respectively. Due to the constraint of the molten pool by the copper blocks, the solidified beads became narrower and taller than those of the NC wall. The contact areas between the two copper blocks and the fabricated walls for AC-W11 and AC-W8 ranged from 1140–3230 mm$^2$ and 1900–4750 mm$^2$, respectively.

### *Microstructural and tensile analysis*

Fig. 3 illustrates an overview of the microstructural and tensile property analysis procedures. Tensile specimens were extracted by electrical discharge machining (EDM) along the build and travel directions (Fig. 3a). These corresponded to No. 14B proportional test pieces compliant with JIS Z2241 (Fig. 3b), with at least four specimens tested for each condition. Tensile tests were conducted at room temperature using a universal testing machine (Z100 THW 100 kN, Zwick Roell GmbH & Co. KG) at a crosshead speed of 2.0 mm/min. The fractographic features were characterized using SEM (SU5000, Hitachi, Ltd.).

Specimens for microstructural observation were extracted from the center of each wall using EDM, with the observation plane parallel to the XOZ plane (Fig. 3a). The specimens were mounted in resin and polished using SiC paper (#320–#4000) and diamond suspensions (6 μm, 3 μm, and 1 μm). Subsequently, the samples were etched for 5–10 s at room

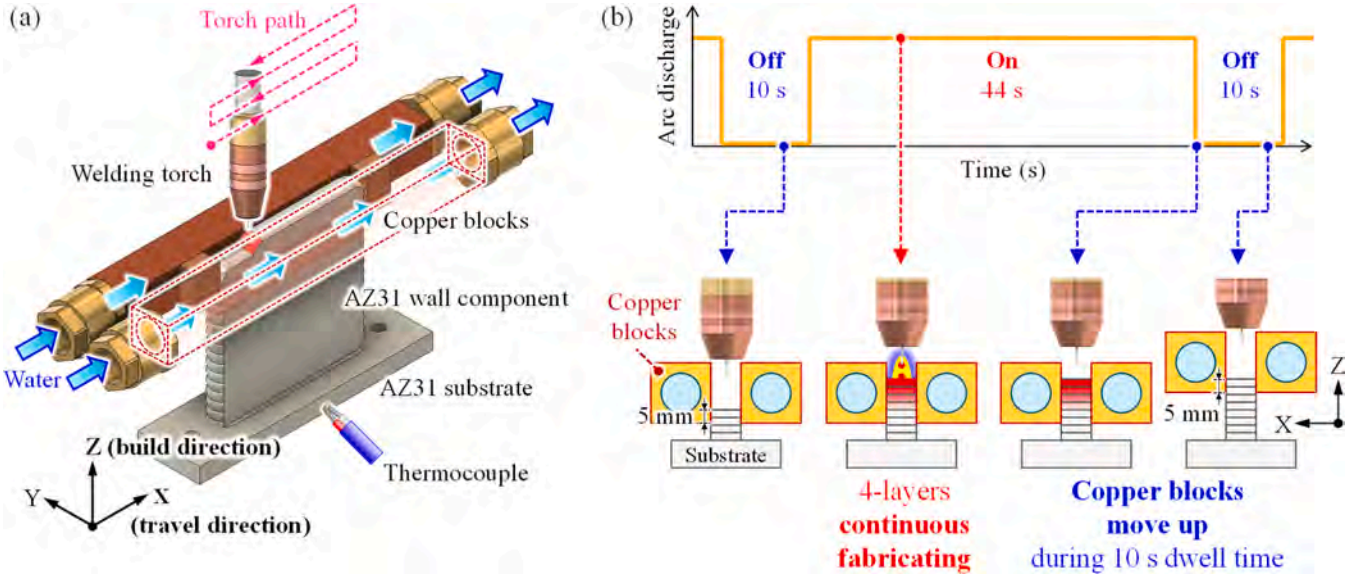


**Fig. 2.** Solid contact-based active cooling (SCAC) system: (a) schematic of SCAC device; (b) fabrication process.

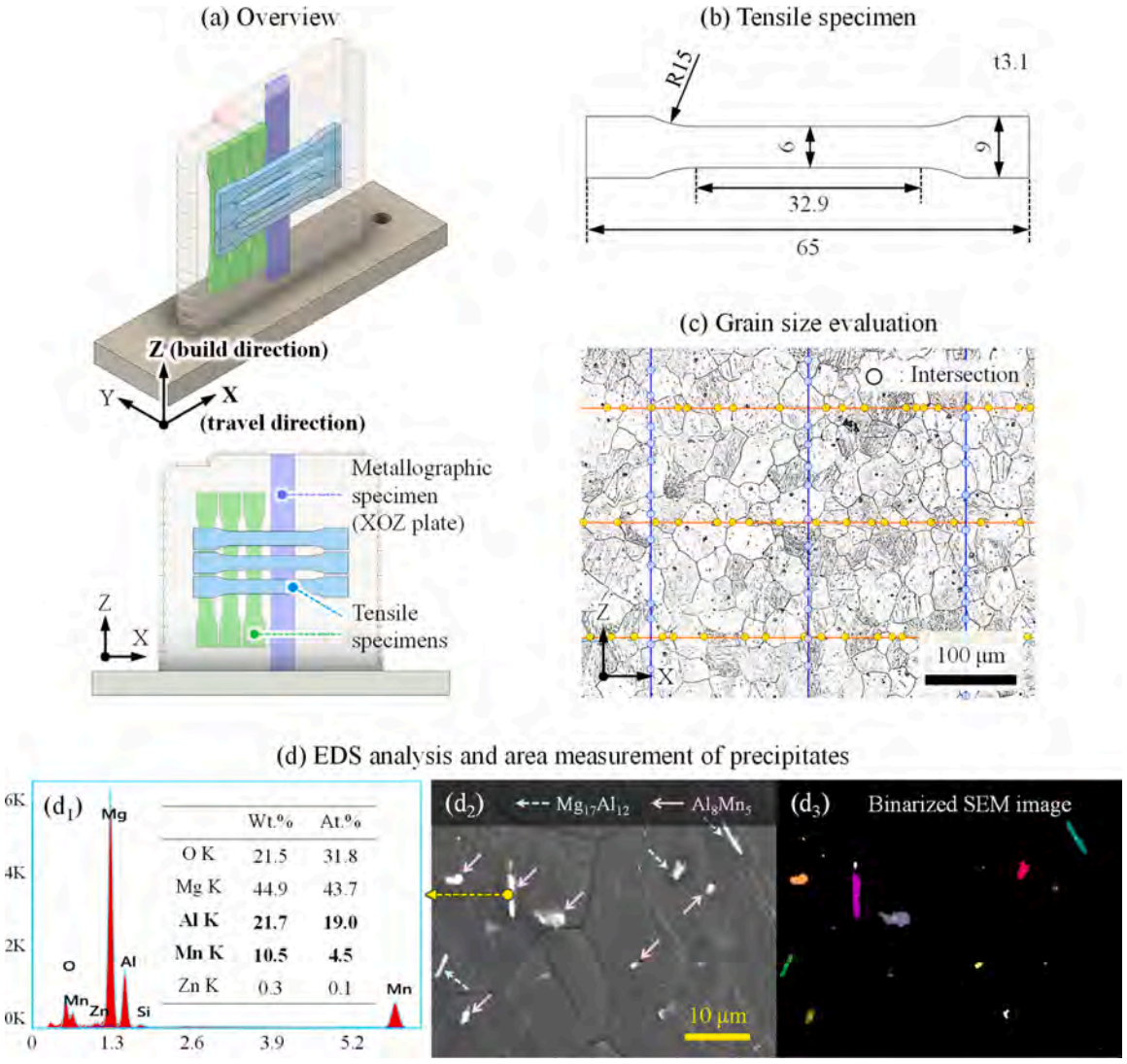


**Fig. 3.** Experimental procedures: (a) sampling positions; (b) geometry of the tensile specimen; (c) grain size evaluation via the intercept method; (d) EDS analysis and measurement of secondary phases.

temperature using a solution comprising 2.5 g picric acid, 2.5 mL acetic acid, 50 mL ethanol, and 5 mL distilled water to reveal grain boundaries and secondary phases. Micrographs were captured using a digital microscope (VHX-6000, Keyence Corp). The grain size was evaluated by the intercept method (JIS G0551) based on the intersections of grain boundaries with test lines drawn parallel to the build height or torch travel direction (Fig. 3c).

As shown in Fig. 3d, precipitates near the center of the build height were analyzed using SEM (VE-8800, Keyence Corp.) equipped with EDS (Element, AMETEK.Inc.). The primary precipitates in AZ31 fabrications (β-$Mg_{17}Al_{12}$ and η-$Al_8Mn_5$) exhibit high brightness in secondary electron images as shown in Fig. $3d_2$ (Nagamatsu and Sasahara, 2026; Yang et al., 2023). The Mg and O peaks detected in EDS spectra are likely attributed to matrix interference, oxidation during air exposure, and instrument resolution limits (Fig. $3d_1$). Therefore, the particles were categorized as follows: $Mg_{17}Al_{12}$ (Al ≥ 8 wt.% and Mn < 3 wt.%) and $Al_8Mn_5$ (Al ≥ 8 wt.% and Mn ≥ 3 wt.%). The cross-sectional area of each precipitate was determined by binarizing 200–300 analyzed particles (Fig. $3d_3$). Considering the instrument resolution, only precipitates with an area of 0.5 μm² or larger were evaluated.

## Results and discussion

### *Dimensional accuracy*

Fig. 4 shows the geometries of the three fabricated walls. 3D scan data were acquired using a 3D coordinate measuring machine (VL300, Keyence Corp.). The color maps indicate the deviation between the average Y-coordinate within the inspection range and the point cloud for each side surface. Deviations of ≤ −0.5 mm (deep concavities) and ≥ 0.5 mm (large convexities) are shown in blue and red, respectively. The side surface roughness ($S_a$) was evaluated using the arithmetic mean height calculated as follows:

$$S_a = \frac{1}{A}\iint_A |y(x,z) - \bar{y}|dxdz \quad (3)$$

The $S_a$ for NC, AC-W11, and AC-W8 were 358 μm, 73 μm, and 66 μm, respectively. These results indicate that AC produced smoother surfaces due to the contact between the molten Mg and the copper blocks (Figs. 4d–f). According to the 3D scan data, the side surface roughness of NC increased with the build height (Fig. 4a). This trend is attributed to the increased build height moving the arc further from the substrate, thereby reducing heat dissipation. Consequently, the temperature

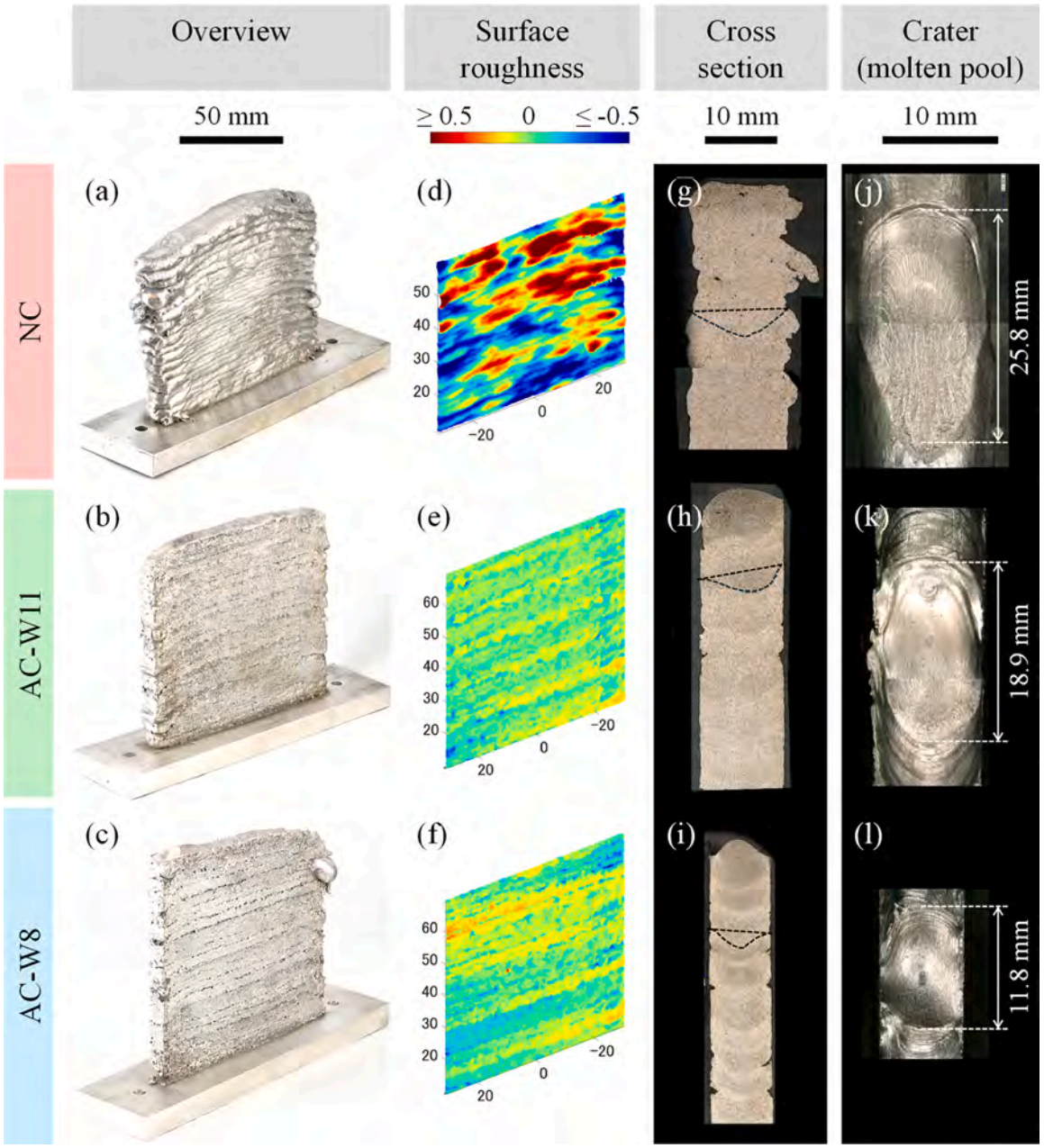


**Fig. 4.** Overview, 3D scan data, cross-sectional views (YOZ plate), crater dimensions of the fabricated thin-walled structures: (a, d, g, j) NC; (b, e, h, k) AC-W11; (c, f, i, l) AC-W8.

around the molten pool rose, leading to bead sagging. The molten pool lengths for NC, AC-W11, and AC-W8 were 25.8 mm, 18.9 mm, and 11.8 mm, respectively (Figs. 4j–l). Furthermore, cross-sectional images reveal that the penetration areas for NC, AC-W11, and AC-W8 were 28.7 $mm^2$, 21.2 $mm^2$, and 10.1 $mm^2$, while the penetration depths were 3.4 mm, 2.5 mm, and 2.0 mm, respectively (Figs. 4g–i). The contact area in AC-W8 was approximately 1.4 times larger than that in AC-W11. This suggests that the expanded contact area enhanced the cooling rate, which likely led to the reduction in molten pool volume.

*Temperature history of the substrate*

Fig. 5 shows the substrate temperature histories measured with K-type thermocouples. The pink areas in Figs. 5a, c, d represent the arc-on periods. Figs. 5a, b illustrate the temperature histories during the deposition of the 2nd and 10th layers for NC. In the 1st layer (Fig. 5a), the substrate temperature reached 248 °C immediately after the torch passed the measurement point, subsequently decreasing to an inter-pass temperature of approximately 57 °C. In the subsequent layers, the peak temperature remained relatively constant between 250 °C and 270 °C (Fig. 5b) as the distance between the arc and the substrate increased. However, the inter-pass temperature rose from 57 °C in the 1st layer to 171 °C in the 10th layer. This indicates that the 120 s interval was insufficient to dissipate the accumulated heat, meaning that heat input exceeded thermal dissipation. This phenomenon prolonged the fluidity of the molten Mg, leading to molten pool enlargement and decreased geometric accuracy due to bead sagging.

Figs. 5c, d show the temperature histories during the fabrication of the 4th and 12th layers for AC-W11 and AC-W8, respectively. Fig. 5c also includes the temperature history for NC during continuous fabrication up to the 4th layer. The slight shifts in the temperature peaks between processes are attributed to the torch elevation at the start and

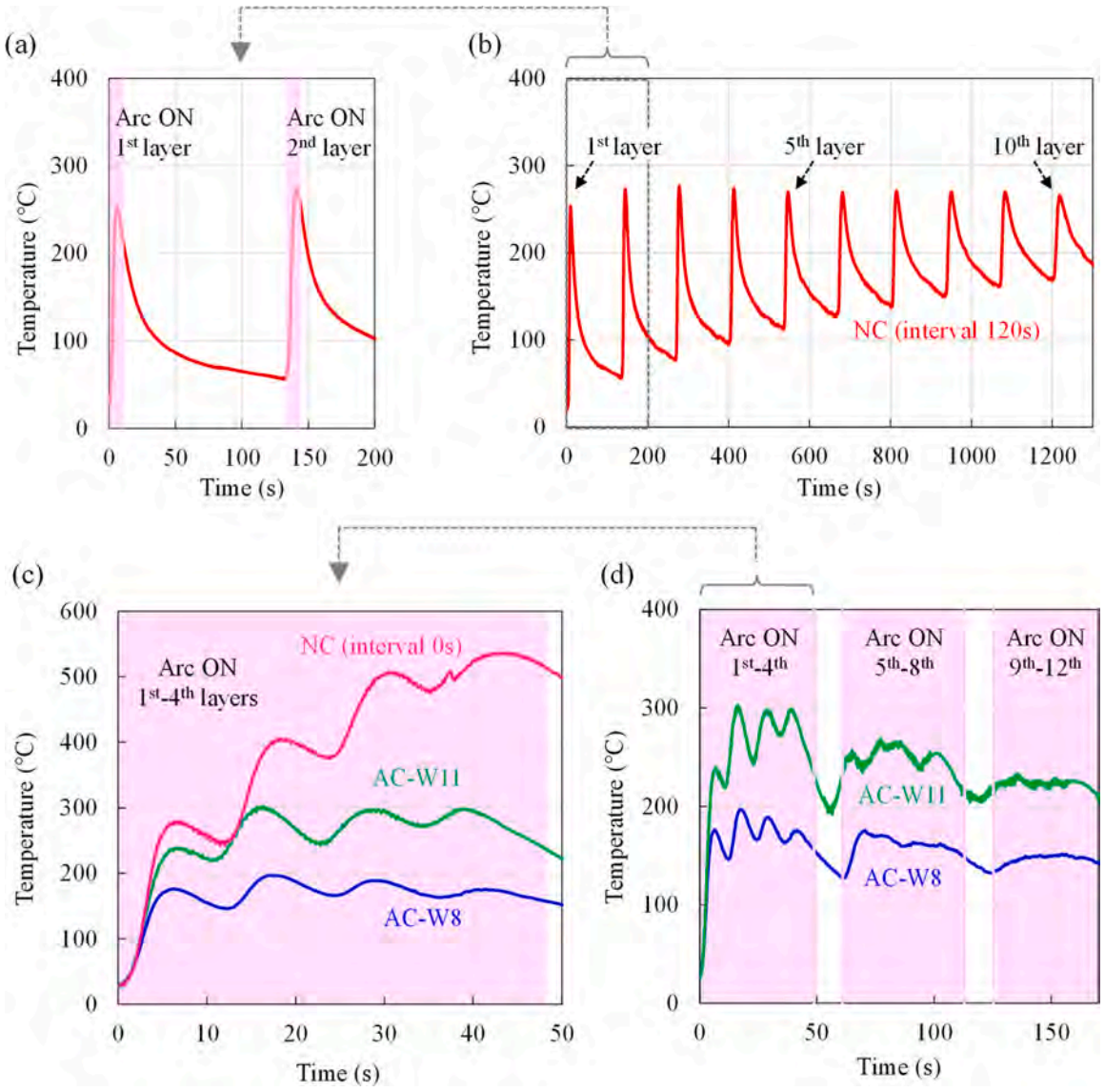


**Fig. 5.** Substrate temperature histories measured by K-type thermocouples: (a, b) 1st to 10th layers in NC; (c) comparison between NC and AC at 0 s interval; (d) 1st to 12th layers in AC.

end of the beads. In the continuous fabrication of NC, the substrate temperature increased with the number of layers, reaching 533 °C. In contrast, during the continuous fabrication of the 1st to 4th layers, the peak temperatures for AC-W11 and AC-W8 were limited to 237–296 °C and 171–195 °C, respectively (Fig. 5c). Furthermore, the disappearance of the distinct peaks and valleys in the temperature histories during the 5th-12th layers indicates that the heat input and heat dissipation reached an equilibrium (Fig. 5d). Although these results do not represent direct temperature measurements of the molten pool, they suggest that AC, particularly AC-W8, effectively mitigated heat accumulation and improved the cooling rate of the fabricated walls.

*Microstructure*

Fig. 6 illustrates the cross-sectional images of the fabricated walls along with the grain size evaluation. Figs. 6a–c present the cross-sections at the center of each wall. A distinct boundary between the heat-affected zone (HAZ) and fusion zone (FZ) was observed in all specimens; the HAZ comprised coarse grains and the FZ featured finer grains. Figs. 6d–f show the grain size distributions in the build direction, evaluated from 500–750 grains within the range of ±3 mm from the wall center. The average grain sizes for NC, AC-W11, and AC-W8 were 46 μm, 28 μm, and 29 μm, with maximum grain sizes of 227 μm, 121 μm, and 124 μm, respectively.

Fig. 6g shows the grain size measurements along the build and travel directions, with 80–125 grains evaluated at each position, where the error bars represent the standard errors. These results indicate that the entire structure was refined by AC. Regarding grain morphology, NC exhibited a columnar structure aligned with the build direction, whereas AC promoted an equiaxed structure. This difference in growth morphology was observed throughout the entire build height. In the height range of 20–40 mm, the grain aspect ratios (the ratio of grain size in the build direction to that in the travel direction) for NC, AC-W11, and AC-W8 were 1.26, 1.03, and 1.06, respectively.

This microstructural evolution is attributed to the temperature gradient ($G$) and solidification rate ($R$). Higher cooling rates ($G \times R$) promote grain refinement, while a lower $G/R$ ratio at the liquid-solid interface facilitates equiaxed grain formation (Ma et al., 2025). In NC, the primary heat dissipation paths are conduction through the deposited layers and surface radiation. Due to inefficient heat extraction, both $G$ and $R$ around the molten pool remain low. However, since heat transfer toward the substrate (Z-axis) predominates, $G$ remains high along the

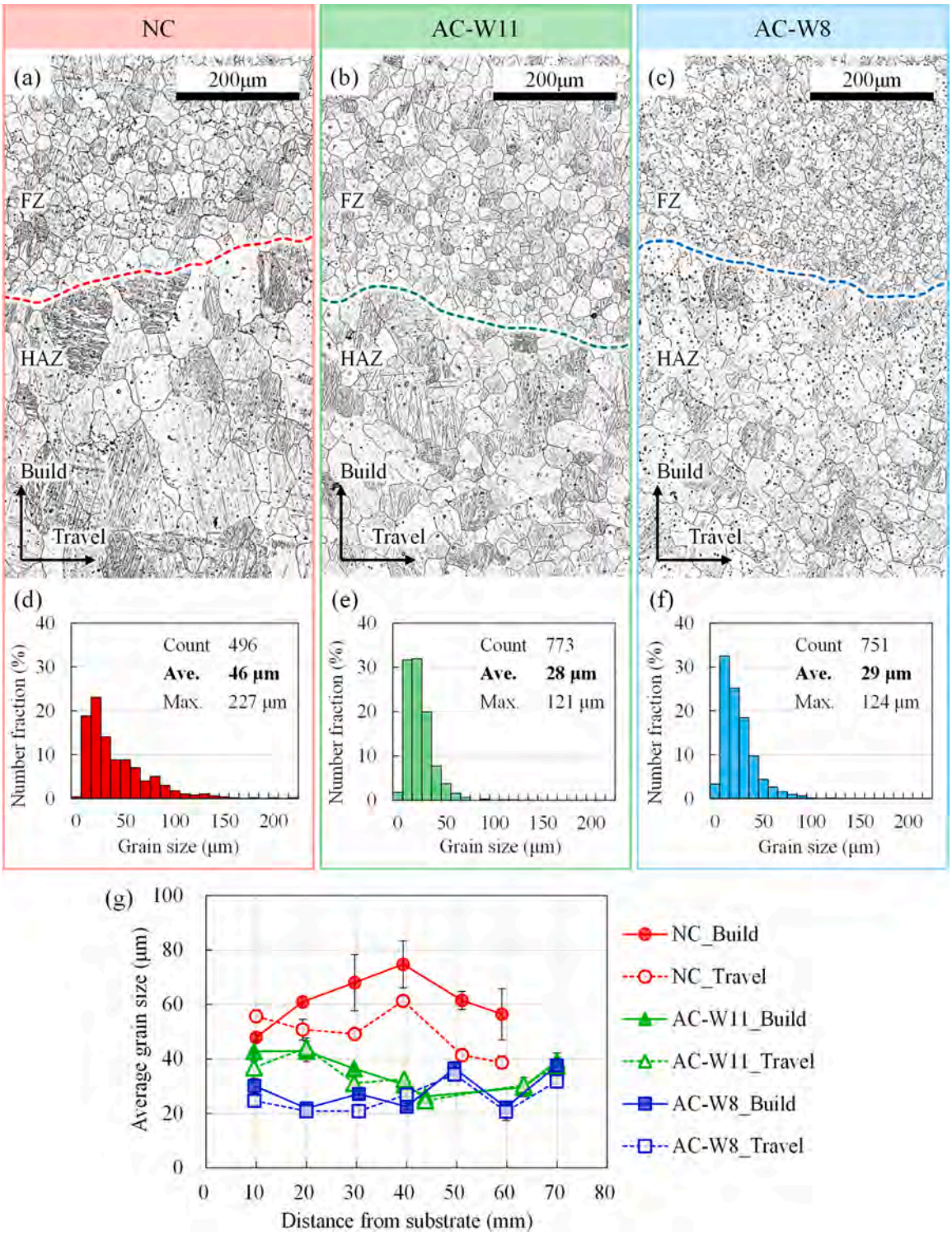


**Fig. 6.** Grain size analysis of the wall components: (a–c) microstructures at the boundary between the HAZ and the FZ; (d–f) number fraction maps; (g) average grain size distribution along the build direction.

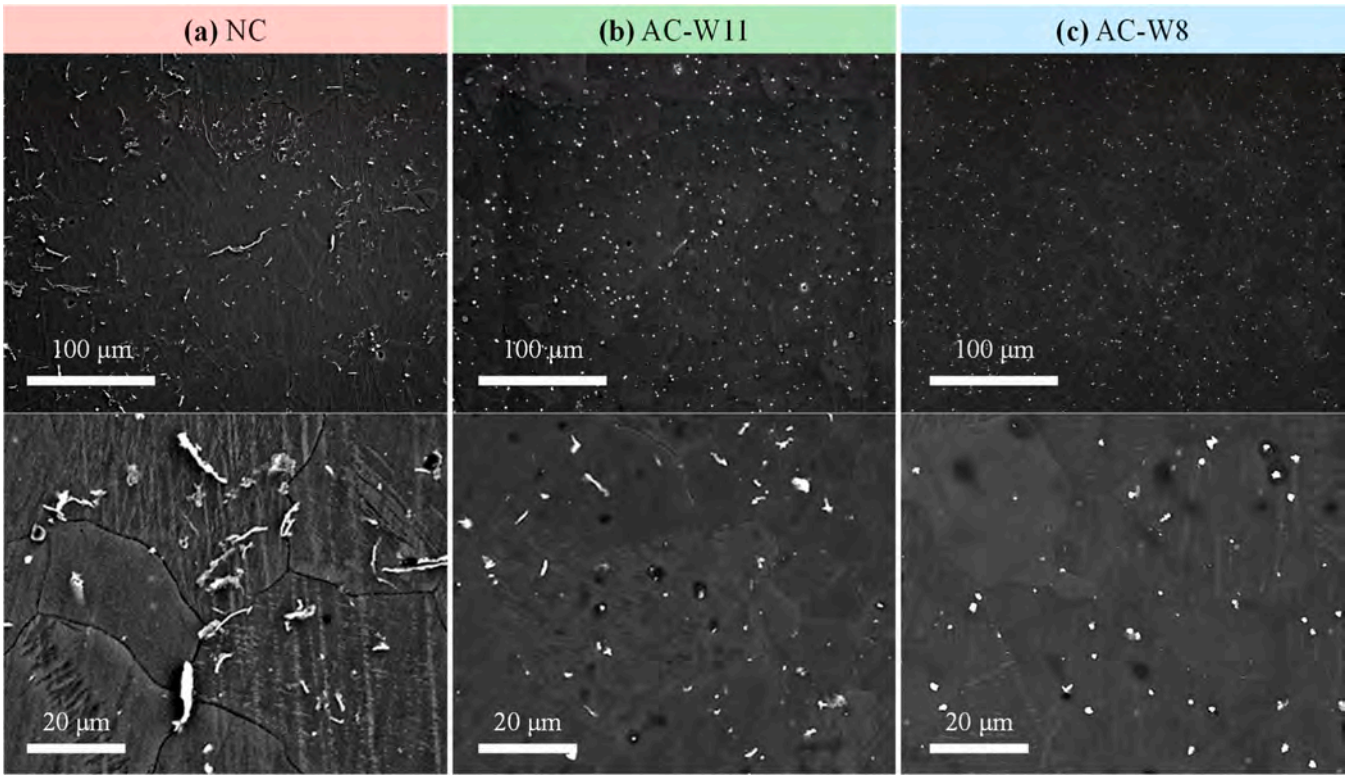


**Fig. 7.** SEM images of (a) NC, (b) AC-W11 and (c) AC-W8.

building direction. Consequently, low $G \times R$ causes grain coarsening, while the directional $G$ leads to columnar grains (Savage and Aronson, 1966).

In contrast, the grain refinement in AC indicates that active cooling via the copper blocks effectively mitigated heat accumulation from shortened inter-pass intervals. This implies that $G$ and $R$ increased even under continuous deposition conditions. Furthermore, lateral (Y-axis) heat dissipation mitigated the directivity of $G$. The significant increase in $R$ relative to $G$ lowered the $G/R$ ratio, promoting equiaxed grain formation. Additionally, as shown in Figs. 5b and 5d, the peak substrate temperature for AC-W11 at a height of ~20 mm (266 °C, 7th layer) was nearly identical to that for NC (264 °C, 10th layer). Nevertheless, Fig. 6g reveals that the grain size of AC-W11 was smaller than that of NC. This suggests that even with a temporary rise in substrate temperature, AC accelerated the cooling rate within the recrystallization temperature range (above 300 °C), effectively suppressing excessive grain growth driven by residual heat after recrystallization (Yang et al., 2024).

Fig. 7 shows the SEM images at the central plane along the build direction. In NC, long strip-shaped precipitates were observed both within the grains and at the grain boundaries. In contrast, fine granular precipitates predominated in AC.

Fig. 8 presents SEM images of representative precipitates in NC and AC-W8, along with the number of detected precipitates and their cross-sectional area fractions by size range. The average cross-sectional areas of the precipitates in NC and AC-W8 were 5.7 μm² and 1.4 μm², respectively. In NC, long strip-shaped $Mg_{17}Al_{12}$ with a maximum area of 97.3 μm² (Fig. 8d) and massive $Al_8Mn_5$ of 59.6 μm² (Fig. 8e) were observed, whereas no precipitates exceeding 10 μm² were confirmed in AC-W8. The number fractions of $Al_8Mn_5$ and $Mg_{17}Al_{12}$ were 77% and 23% for NC (Figs. 8a, b), and 78% and 22% for AC-W8 (Fig. 8c), showing a similar trend. However, the total area fractions of $Al_8Mn_5$ and $Mg_{17}Al_{12}$ were 58% and 42% for NC, compared to 78% and 22% for AC-W8. This difference in NC is attributed to the extensive precipitation of strip- or rod-like $Mg_{17}Al_{12}$ exceeding 10 μm², which alone accounted for 48% of the total area fraction.

Li et al. (2023) reported that AC leads to the refinement of precipitates. Regarding precipitation behavior, Goka et al. (2024) reported that higher cooling rates shorten the time available for nucleation and growth, thereby suppressing the coarsening of $Mg_{17}Al_{12}$. Yang et al. noted that α-Mg and $Al_8Mn_5$ begin to precipitate when the molten pool temperature drops below 650 °C, while $Mg_{17}Al_{12}$ forms below 350 °C (Yang et al., 2024, 2023). Since large precipitates are prone to fracture and act as crack initiation sites during loading, leading to premature failure (Huang et al., 2018), it is considered that AC improved the cooling rate specifically in the low-temperature range (below 350 °C). This effectively suppressed the formation of coarse $Al_8Mn_5$ and $Mg_{17}Al_{12}$ that otherwise would act as crack initiation sites.

### *Tensile properties*

Table 4 and Fig. 9 show the representative tensile test results, while all tensile data are summarized in Table A.2 and Fig. A.1. The values presented in Table 4 and Fig. 9 are the averages, with error bars representing the standard errors. The statistical significance of the differences between the mean values of the NC and AC conditions was evaluated using Welch's *t*-test, where a *p*-value of less than 0.05 was considered statistically significant. Furthermore, the stress-strain curves are plotted using representative data closest to the average for each condition.

In the build direction, the averages of the yield strength (YS), ultimate tensile strength (UTS), and elongation (EL) exhibited slight increases of 5 MPa, 9 MPa, and 3%, respectively, by employing AC. However, the *p*-values for YS, UTS, and EL were 0.039, 0.10, and 0.50, respectively, indicating that the differences in UTS and EL were not statistically significant. In the travel direction, similar increases of 12 MPa, 13 MPa, and 10% were observed for YS, UTS, and EL, respectively. The corresponding *p*-values were 0.001, 0.039, and 0.030, confirming that all these increases were statistically significant.

To investigate the cause of the lack of statistical significance in the tensile properties along the build direction, fractographic observation

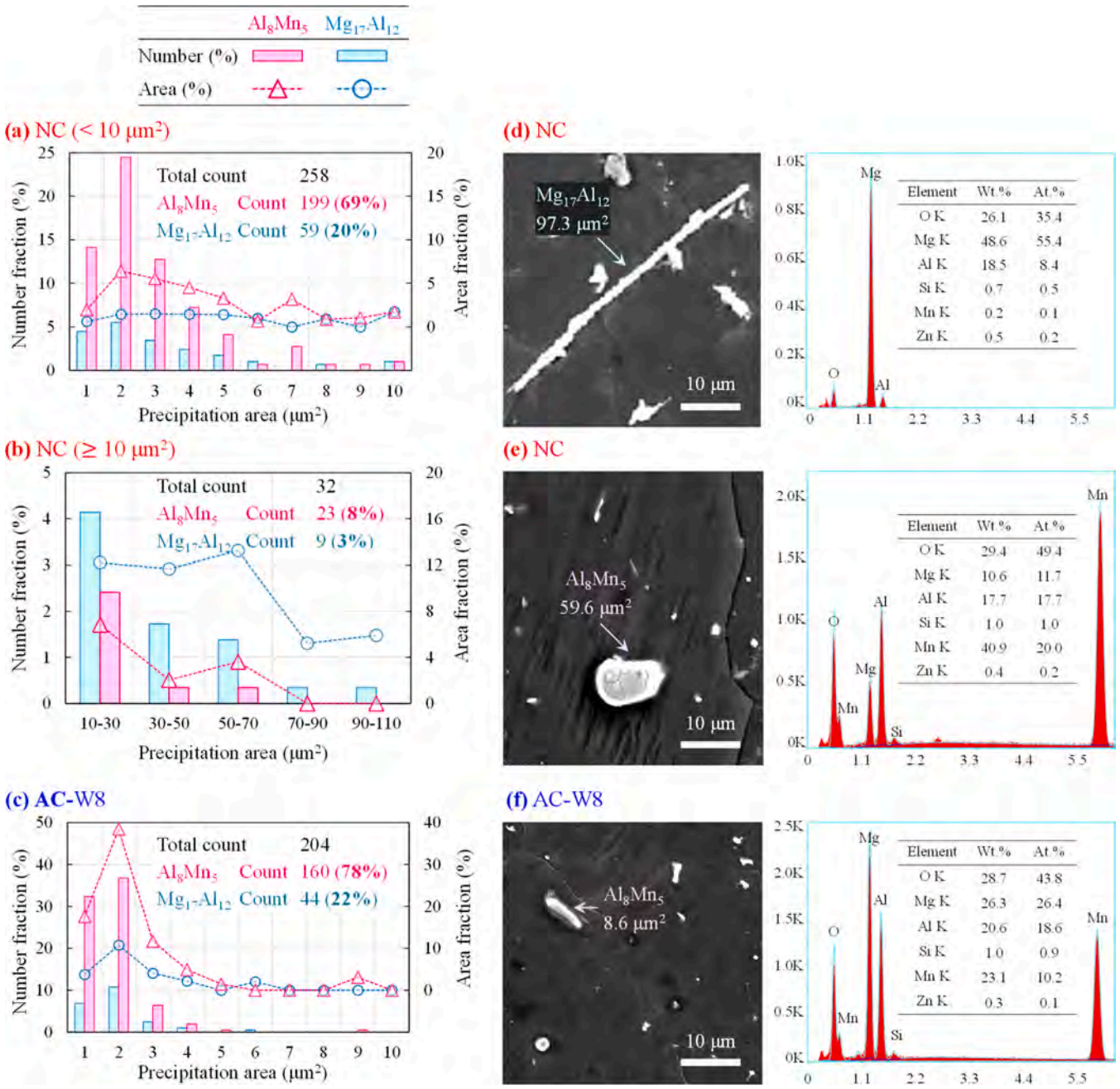


**Fig. 8.** Number and area fractions of the secondary precipitates: (a) NC for area under 10 μm²; (b) NC for area 10 μm² or more; (c) AC-W8 for all size ranges. SEM images showing maximum sizes of (d) $Mg_{17}Al_{12}$ and (e) $Al_8Mn_5$ in NC, and (f) $Al_8Mn_5$ in AC-W8.

was conducted on the AC-W8 specimens that exhibited the lowest and higher tensile strengths (Fig. 10). Macro-scale observation (Figs. 10a, d) revealed distinct black regions on the fracture surface, which were particularly pronounced in the lowest-strength specimen (indicated by yellow arrows). While the total projected area of these regions was only 0.5% of the original cross-sectional area in the higher-strength specimen, it accounted for approximately 2.7% in the lowest-strength specimen. High-magnification observation (Figs. 10b, c, e, f) confirmed that these regions consisted of agglomerated smut, which is characterized as a Mg-Al-O amorphous layer containing nano-sized MgO particles (Sugiyama et al., 1993).

Generally, smut does not directly degrade tensile strength. However, in the SCAC process used in this study, where the welding zone is enclosed by copper blocks, a large amount of smut tends to remain within the confined space. Furthermore, during this process, the molten pool often flows ahead of the arc in the torch travel direction. Since the melting point of MgO (2852 °C) is extremely high compared to the boiling point of Mg (1090 °C), these oxide particles could potentially remain as solid inclusions within the molten pool. Consequently, the layered smut accumulation, which aligned parallel to the travel direction, increased the unbonded regions, leading to early yielding. Additionally, microvoids nucleating at these smut interfaces could have coalesced prematurely, potentially inducing premature brittle fracture and consequently reducing UTS and EL.

Tensile results along the travel direction indicate that both strength and elongation increased in the order of AC > NC, which is consistent with previous studies reporting enhanced tensile properties due to grain refinement (Chapman and Wilson, 1962; Hauser et al., 1956). The superior strength and ductility in the travel direction compared to the build direction are attributed to the alignment of the FZ and HAZ

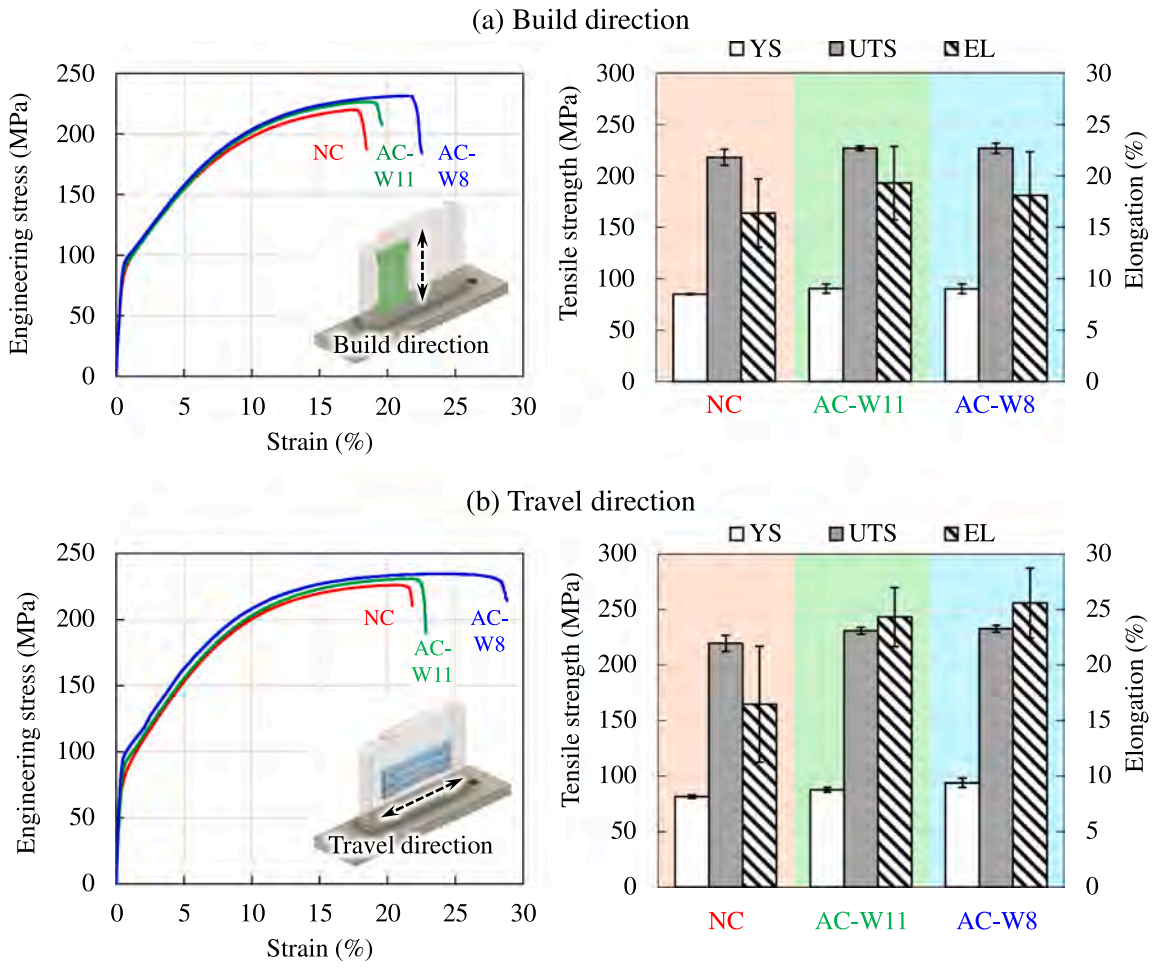


**Fig. 9.** Engineering stress-strain curves and summarized tensile properties: (a) build and (b) travel directions.

**Table 1**
Nominal chemical composition of the AZ31 magnesium alloy wire (in Wt.%).

| Al | Zn | Mn | Fe | Si | Cu | Ni | Ca | Other | Mg |
|---|---|---|---|---|---|---|---|---|---|
| 2.4–3.6 | 0.50–1.5 | 0.15–1.0 | ≤0.005 | ≤0.10 | ≤0.05 | ≤0.005 | ≤0.04 | 0.05–0.30 | Bal. |

**Table 2**
Physical properties of the cooling copper blocks (equivalent to JIS C1100P).

| Properties | Unit | Value |
|---|---|---|
| Specific heat | J/(kg·K) | 385 |
| Coefficient of expansion | $10^{-6}$ K | 17.7 |
| Thermal conductivity | W/(m·K) | 391 |
| Electroconductivity | %IACS | ≥97 |
| Liquidus temperature | °C | 1083 |
| Solidus temperature | °C | 1065 |

**Table 3**
Processing parameters.

| | | NC | AC-W11 | AC-W8 |
|---|---|---|---|---|
| Cooling convention | - | NC | SCAC | SCAC |
| Space between copper blocks *W* | mm | - | 11.3 | 8.2 |
| Welding mode | - | DC-pulse | DC-pulse | DC-pulse |
| Welding current | A | 132 | 132 | 132 |
| Welding voltage | V | 22.1 | 22.1 | 22.1 |
| WFS | m/min | 16.0 | 16.0 | 16.0 |
| DR | $cm^3/h$ | 1086 | 1086 | 1086 |
| Ave. $T_{dwell}$ | s | 120 | 2.5 | 2.5 |
| MR | $cm^3/h$ | 90 | 882 | 882 |
| TS | mm/min | 500 | 500 | 500 |
| Bead length | mm | 90 | 90 | 90 |
| Bead height | mm | 2.0 | 2.8 | 3.8 |
| Number of layers | - | 40 | 32 | 24 |
| Wall height | mm | 80 | 90 | 90 |

parallel to the loading direction (Wang et al., 2021).

The increase in YS is generally attributed to three main strengthening mechanisms: grain boundary strengthening, precipitation strengthening, and solid solution strengthening. The contribution of grain boundaries to YS ($\Delta\sigma_{GB}$) can be estimated using the Hall-Petch equation:

$$\Delta\sigma_{GB} = kd^{-0.5} \quad (4)$$

where $k$ represents Hall-Petch coefficient ($k$ = 281 MPa μm$^{1/2}$ (Yuan et al., 2011)) and $d$ denotes average grain diameter. As shown in Figs. 6d–f, the average grain sizes at the wall center within the gauge length for NC and AC-W8 were 46 μm and 29 μm, respectively. Thus, the increase in $\Delta\sigma_{GB}$ of AC is estimated to be ~ 10.7 MPa, indicating that

**Table 4**
Tensile properties (average ± standard error) of the NC and AC components.

| Cooling strategy | Tensile direction | Number of samples *n* | YS (MPa) | UTS (MPa) | EL (%) |
|---|---|---|---|---|---|
| NC | Build | 4 | 85 ± 1 | 218 ± 8 | 16 ± 3 |
| AC-W11 | Build | 4 | 90 ± 5 | 227 ± 2 | 19 ± 4 |
| AC-W8 | Build | 6 | 90 ± 5 | 227 ± 5 | 18 ± 4 |
| NC | Travel | 4 | 82 ± 1 | 220 ± 7 | 16 ± 5 |
| AC-W11 | Travel | 7 | 88 ± 2 | 231 ± 4 | 24 ± 4 |
| AC-W8 | Travel | 5 | 94 ± 4 | 233 ± 3 | 26 ± 3 |

grain refinement is the dominant factor in YS increase under the current fabrication conditions. Regarding the limited contribution of precipitation strengthening, Ma et al. (2025) reported that nano-sized precipitates ($Al_8Mn_5$, $Mg_{17}(Al, Zn)_{12}$) formed by AC contributed to a 33.4 MPa increase in the YS of AZ31 walls. This discrepancy is likely attributable to the fabrication parameters. The current and voltage used by Ma et al. (90 A, 12.3 V) were lower than those in this study (132 A, 22.1 V), and their inter-pass interval (approximately 70 s per layer) was longer. Our continuous fabrication with higher heat input may have extended the residence time within the temperature range for precipitate growth (350–650 °C), leading to the coarsening of precipitates to sub-micron scales that do not effectively contribute to precipitation strengthening (Yang et al., 2024). Although nano-scale precipitates were not evaluated via transmission electron microscopy (TEM) in this study, the relationship between heat input and precipitation strengthening in AC warrants further investigation. Regarding solid solution strengthening, Yang et al. (2023) stated that its contribution to the YS of AZ31 is small as it is a low-alloy Mg. Furthermore, Ma et al. (2025) noted that even with AC, the effect of solid solution strengthening is weakened because solute atoms are consumed by the formation of numerous precipitates. Therefore, the contribution of solid solution strengthening in AC is considered limited compared to grain boundary and precipitation strengthening.

The increase in elongation with AC can be attributed to several factors. In Mg alloys, grain refinement increases deformation uniformity, thereby enhancing ductility (Kobayashi et al., 2003; Koike et al., 2003; Yoshida et al., 2005). Furthermore, the elongation along the travel direction tended to be higher than that along the build direction. This is because the FZ is distributed more continuously in the travel direction. This continuity helps maintain strain compatibility, increasing the work-hardening capacity required to maintain deformation uniformity, and leading to enhanced ductility (Kobayashi et al., 2003).

Fig. 11 shows the fracture surfaces of the tensile specimens along the build direction for NC and AC-W8. Although macroscopic necking occurred in both specimens, the fracture surface of NC was relatively flat, whereas that of AC-W8 exhibited significant ridges (Figs. 11a, e).

The NC specimen primarily consists of multiple flat facets, with localized deep cracks (indicated by blue arrows) and shallow dimples (Figs. 11b, c). Clear unidirectional river patterns were observed within each facet, with their extension directions changing discontinuously at facet boundaries. This morphology suggests that the crack traversed the grain interiors along specific crystallographic planes, rather than propagating along grain boundaries. This transgranular path is consistent

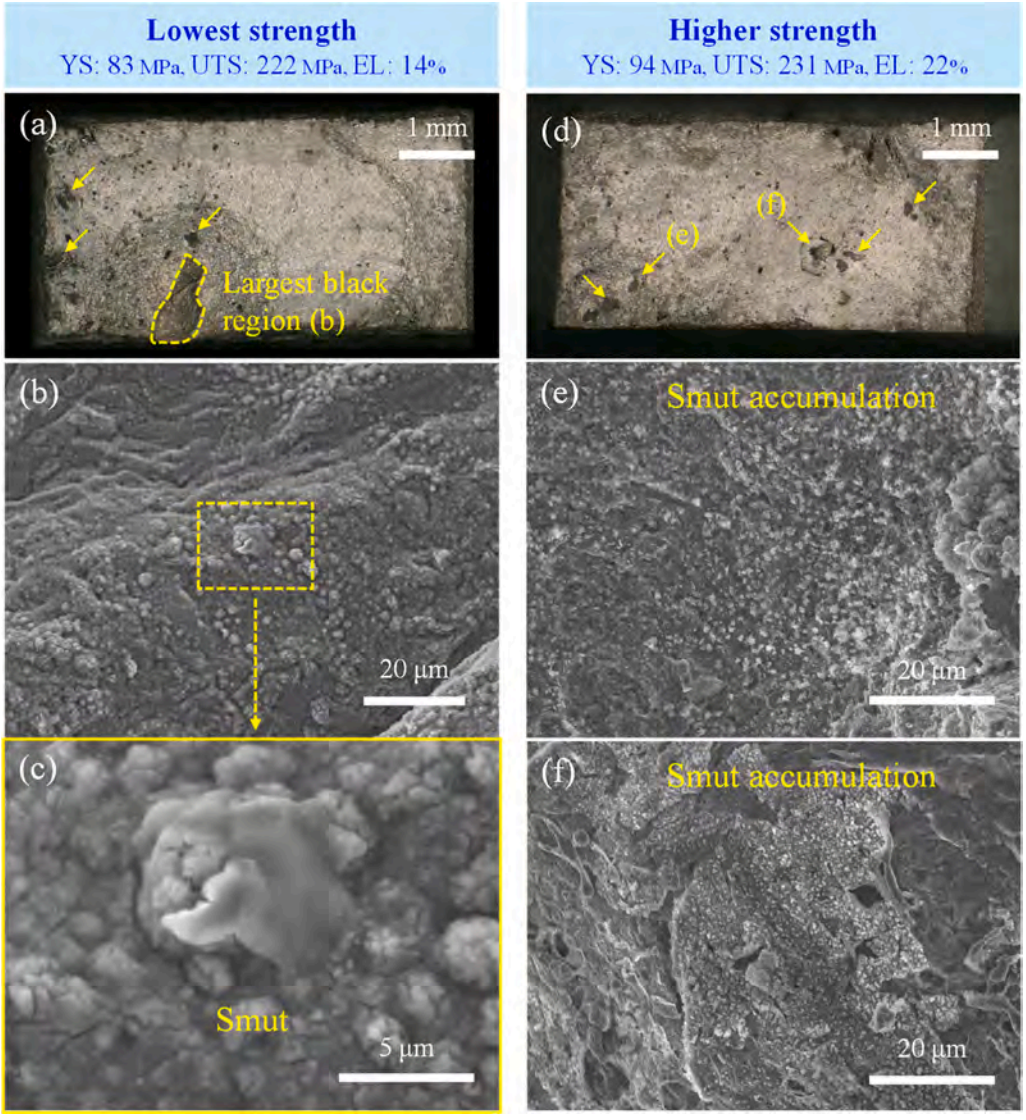


**Fig. 10.** Fractographs of the AC-W8 specimens along the build direction: (a–c) lowest-strength specimen, showing macro-surface with black regions and high-magnification views of agglomerated smut; (d–f) higher-strength specimen, showing macro-surface and corresponding localized smut accumulations.

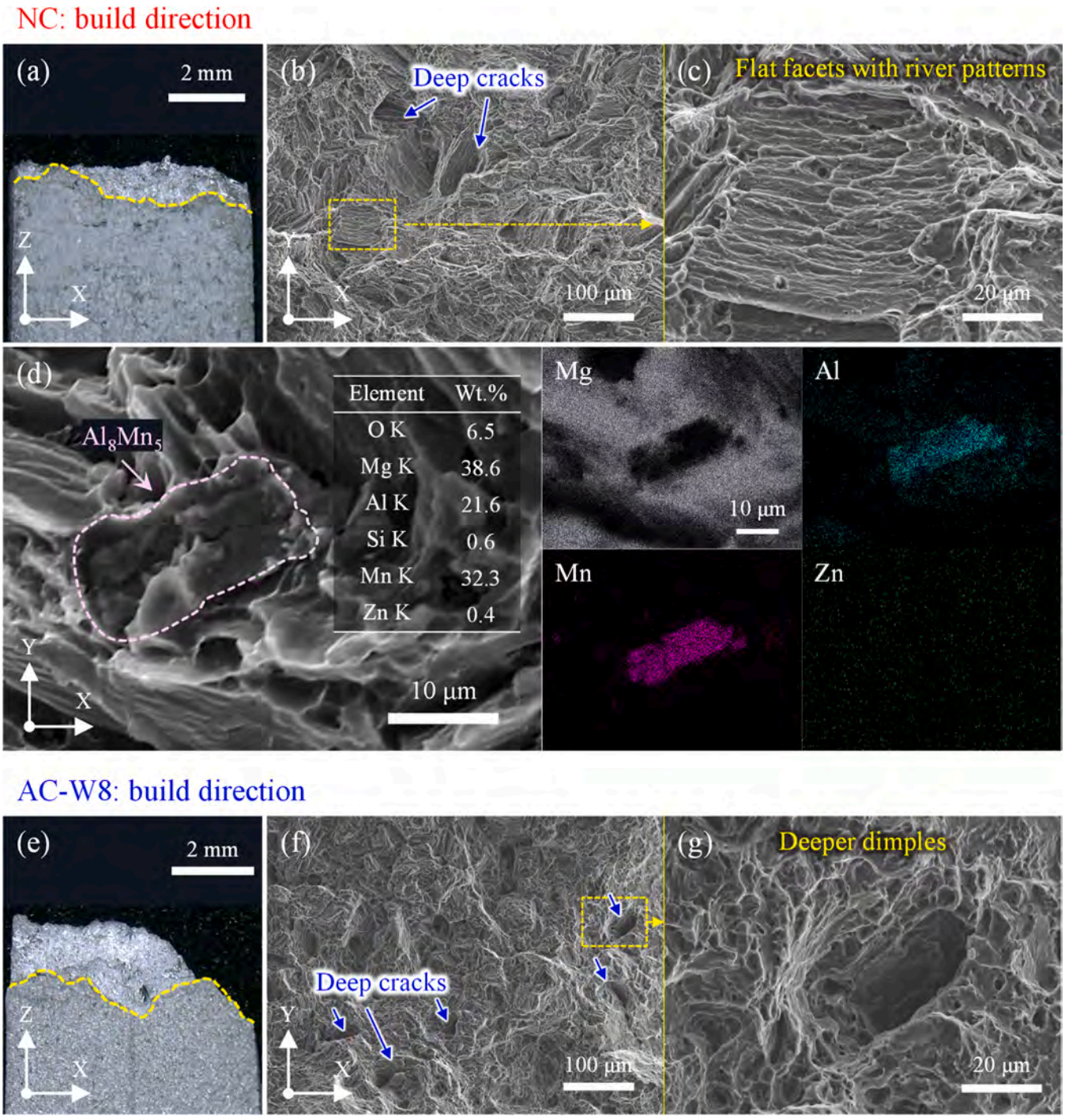


**Fig. 11.** Tensile fractures in the build direction: (a–d) NC and (e–g) AC-W8. (a, e) Side views; (b, c, f, g) SEM images; (d) EDS map.

with a quasi-cleavage fracture mode (Li et al., 2023). Furthermore, coarse $Al_8Mn_5$ precipitates (projected area > 100 μm$^2$) were observed on the fracture surface (Fig. 11d). It is inferred that these coarse particles acted as stress concentrators, initiating microscopic internal cracks that propagated rapidly through the coarse grains, leading to the quasi-cleavage appearance.

In contrast, flat facets are limited in the AC specimen, where a mixture of dimples of various sizes and deep cracks was confirmed across the entire fracture surface (Fig. 11f). This morphological transition is attributed to the altered crack path resulting from grain refinement. The increased grain boundary density effectively inhibited linear crack extension and induced significant crack deflection, creating a highly convoluted surface with prominent ridges (Fig. 11e). The deep cracks represent the coalescence of internal voids during necking (Fig. 11g), suggesting that the refined microstructure accommodated extensive plastic deformation prior to final failure (Goka et al., 2024; Wang et al., 2022).

Therefore, the results suggest that active cooling promoted a transition from a predominantly quasi-cleavage mode to an extensive ductile fracture mode, effectively leveraging the enhanced plasticity of the refined grains.

Fig. 12 presents the fracture surfaces of the tensile specimens along the travel direction. To correlate the fracture morphology with the microstructure, the side surface was polished and etched at a position

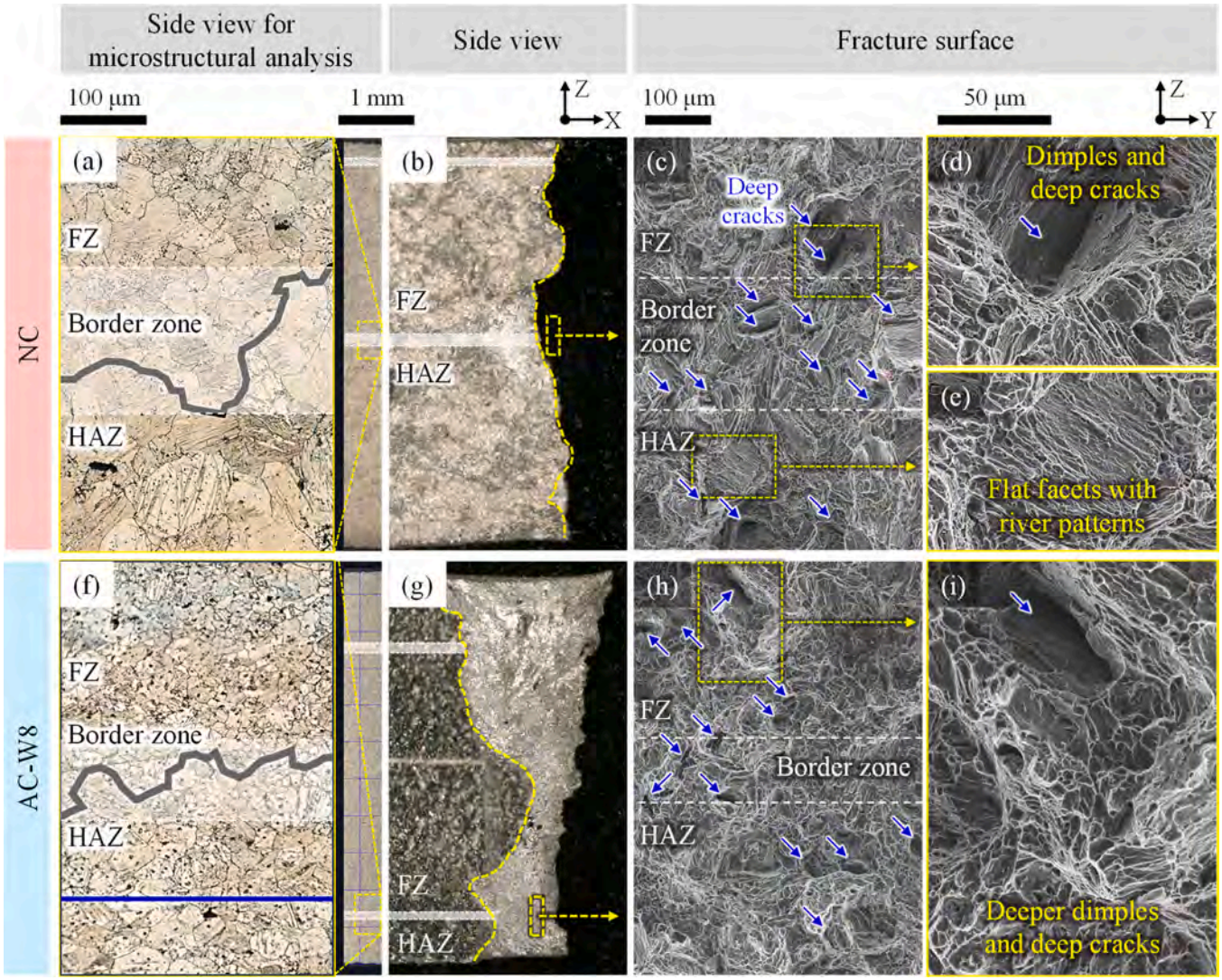


**Fig. 12.** Tensile fractures in the travel direction: (a–e) NC and (f–i) AC-W8. (a, f) Microstructures at the boundary between the HAZ and the FZ; (b, g) side views; (c–e, h, i) SEM images.

offset by 15 mm to identify the approximate location of the FZ-HAZ boundary (Figs. 12a, f).

Consistent with the observations in the build direction, the NC fracture surface was relatively flat (Fig. 12b), while that of AC-W8 exhibited significant ridges (Fig. 12g). In the NC specimen, the fracture morphology appeared to vary depending on the region (Fig. 12c). Within the HAZ, flat facets with unidirectional river patterns appeared to be more prevalent (Fig. 12e), whereas the FZ was more frequently associated with dimples and deep cracks (Fig. 12d). In contrast, while the FZ side in AC-W8 also featured deep dimples and cracks (Figs. 12h, i), the morphological disparity between the HAZ and FZ appeared to be less pronounced than in the NC specimen. These observations indicate that AC effectively suppressed the microstructural heterogeneity between the FZ and HAZ. While the NC specimen suffered from localized brittle fracture within the coarse-grained HAZ, the refined and uniform grain structure in the AC-W8 specimen promoted consistent deformation behavior across both regions, thereby reducing the morphological disparity on the fracture surface.

## Conclusions

In this study, AZ31 thin-wall structures were fabricated at an extremely high manufacturing rate (MR) of 882 $cm^3$/h using a wire-arc DED system with solid-contact active cooling (SCAC). SCAC significantly increased the MR compared to natural cooling (NC) at 90 $cm^3$/h, while successfully maintaining or slightly increasing the tensile properties. These results demonstrate that active cooling (AC) dramatically increases MR without compromising material properties. The major conclusions are summarized below.

1. In NC, bead sagging occurred in the upper layers, whereas AC yielded smooth side surfaces due to contact with the copper blocks. Furthermore, narrowing the gap between the copper blocks reduced the molten pool volume.
2. In NC, the substrate inter-pass temperature rose despite a 120 s interval. In contrast, AC maintained lower peak and inter-pass temperatures than NC, average inter-pass interval of only 2.5 s.
3. AC refined the average grain size from 46 μm to 28 μm and the average area of precipitates ($Mg_{17}Al_{12}$ and $Al_8Mn_5$) from 5.7 $\mu m^2$ to 1.4 $\mu m^2$. In the AC structures, $Al_8Mn_5$ predominated, and the coarse precipitates (10–97 $\mu m^2$) observed in NC were not detected.
4. AC slightly increased the YS, UTS, and EL by 5 MPa, 9 MPa, and 3% in the build direction, although no statistically significant differences were observed. This lack of significance is likely attributable to the confined fabrication space unique to SCAC, which potentially

induced the layered smut accumulation and consequently increased unbonded regions.

5. AC increased the YS, UTS, and EL by 12 MPa, 13 MPa, and 10% in the travel direction, with all these increases being statistically significant. The YS enhancement is primarily attributed to grain refinement, as the calculated Hall-Petch contribution (~10.7 MPa) aligns with the experimental results.

6. Fractographic analysis suggests that active cooling promoted a transition from a predominantly quasi-cleavage mode to an extensive ductile fracture mode, leveraging the enhanced plasticity of the refined grains.

## CRediT authorship contribution statement

**Hyu Kudo:** Writing – review & editing, Writing – original draft, Visualization, Validation, Investigation, Formal analysis, Data curation. **Houichi Kitano:** Writing – review & editing, Formal analysis, Data curation. **Hiroyuki Sasahara:** Writing – review & editing, Resources, Conceptualization. **Hideaki Nagamatsu:** Writing – review & editing, Writing – original draft, Visualization, Validation, Supervision, Resources, Project administration, Methodology, Investigation, Funding acquisition, Formal analysis, Data curation, Conceptualization.

## Declaration of competing interest

The authors declare that they have no known competing financial interests or personal relationships that could have appeared to influence the work reported in this paper.

## Acknowledgements

This work was supported by the Japan Welding Engineering Society and the Light Metal Educational Foundation. The authors would like to acknowledge Associate Prof. Y. Shinohara for her insights into metallurgical characterization and J. Kinoshita and T. Kobayashi for his technical support in cooling device development.

## Appendix

**Table A.1**
Comparisons of manufacturing rates for wire-arc DED components.

| Marker in Fig. 1 | Cooling strategy | Material | MR ($cm^3$/h) | DR ($cm^3$/h) | ∅ (mm) | WFS (m/min) | TS (mm/min) | $T_{dwell}$ (s) | $L$ (mm) | Annotation and references |
|---|---|---|---|---|---|---|---|---|---|---|
| △ | NC | AZ31 | 45 | 136 | 1.2 | 2.0 | 200 | 60 | 100 | (Guo et al., 2016) |
| △ | NC | AZ31 | 231 | 611 | 1.2 | 9 | 420 | 60 | 255* | Bead length was calculated from longitudinal dimension, swing width, and swing length (Ma et al., 2023). |
| △ | NC | AZ31 | 58 | 475 | 1.2 | 7.0 | 600 | 180 | 250 | (Wang et al., 2021) |
| △ | NC | WE43 | 189 | 589 | 5.0 | 0.5 | 200 | 70 | 110 | Filler rod was used (Tong et al., 2023). |
| △ | NC | AZ80M | 19 | 139 | 1.6 | 1.15 | 300 | 160 | 130* | The bead length is indicated in Fig. 4 of the cited paper (Guo et al., 2021). |
| △ | NC | ATZM31 | 76 | 835 | 1.2 | 12.3 | 600 | 120 | 120* | The bead length is indicated in Fig. 2 of the cited paper (Yang et al., 2023). |
| △ | NC | AZ31 | 54 | 502 | 1.2 | 7.4 | 498 | 120 | 120 | (Goka et al., 2024) |
| △ | NC | WE43 | 271 | 543 | 1.2 | 8.0 | 600 | 30 | 300 | (Li et al., 2024) |
| △ | NC | ER90S-G | 39 | 1154 | 1.2 | 17 | 900 | 420 | 220 | Fabrication was carried out using a double-wire system (Wang et al., 2023). |
| O | SCAC | AZ31 | 364 | 774 | 1.2 | 11.4 | 300 | 18 | 80 | (Nagamatsu and Sasahara, 2026) |
| O | SCAC | AZ31 | 229 | 421 | 1.2 | 6.2 | 450 | 70* | 100 | Interval was calculated based on 12 layers over 1000 s (Ma et al., 2025). |
| O | SCAC | ER2325 | 88 | 543 | 1.2 | 8 | 400 | 77.8 | 100 | (Li et al., 2018) |
| O | SCAC | Mild steel | 220 | 605 | ? | ? | 800 | 30 | 228 | (Heinrich et al., 2023) |
| O | SCAC | Ti-6Al-4V | 230 | 519 | 1.14 | 8.5 | 700 | 60 | 554 | Fabrication with active cooling applied through the substrate (Vázquez et al., 2020). |
| O | SCAC | AZ31 | 86 | 373 | 1.2 | 5.5 | 400 | 60 | 120 | Active cooling was achieved by cryogenic cooling of the substrate (Li et al., 2023) |
| □ | NC | ER70 | 637 | 1911 | ? | ? | ? | ? | ? | DR is 15 kg/h and MR is 5 kg/h (WAAM3D Limited, 2021). |
| □ | NC | ER4043 | 317 | 317 | 1.2 | 4.67* | 618* | 0 | ? | WFS and TS were the average values calculated from Table 5 of the cited paper (Zhao et al., 2020). |
| ⋄ | Water cooling | ER5356 | 386 | 386 | 1.0 | 8.2 | 450 | 0 | ? | (Da Silva et al., 2020) |
| ⋄ | Water cooling | Stainless | 163 | 271 | 1.2 | 4.0 | 400 | 15 | 150 | (Jorge et al., 2025) |

*Estimated from figures or other available data where explicit values were not provided in the literature.

**Table A.2**
All tensile test results.

| Cooling strategy | Tensile direction | Label | YS (MPa) | UTS (MPa) | EL (%) |
|---|---|---|---|---|---|
| NC | Build | 1 | 84.8 | 222.7 | 18.4 |
| | | 2 | 84.9 | 223.0 | 18.1 |
| | | 3 | 85.5 | 220.1 | 17.6 |
| | | 4 | 84.2 | 206.5 | 11.4 |

(continued on next page)

**Table A.2** (*continued*)

| Cooling strategy | Tensile direction | Label | YS (MPa) | UTS (MPa) | EL (%) |
|---|---|---|---|---|---|
| AC-W11 | Build | 1 | 86.4 | 225.3 | 17.7 |
| | | 2 | 96.7 | 230.3 | 24.5 |
| | | 3 | 88.1 | 225.0 | 16.4 |
| | | 4 | 89.4 | 226.6 | 18.6 |
| AC-W8 | Build | 1 | 93.9 | 231.4 | 21.8 |
| | | 2 | 83.2 | 221.6 | 14.1 |
| | | 3 | 91.8 | 230.0 | 16.5 |
| | | 4 | 91.7 | 232.4 | 24.8 |
| | | 5 | 94.2 | 223.4 | 15.0 |
| | | 6 | 85.5 | 222.3 | 16.3 |
| NC | Travel | 1 | 81.3 | 215.4 | 13.0 |
| | | 2 | 80.7 | 225.1 | 21.1 |
| | | 3 | 80.5 | 226.1 | 20.8 |
| | | 4 | 83.7 | 211.4 | 11.0 |
| AC-W11 | Travel | 1 | 88.6 | 235.6 | 22.5 |
| | | 2 | 84.8 | 225.8 | 23.9 |
| | | 3 | 86.0 | 229.7 | 29.9 |
| | | 4 | 90.9 | 230.9 | 22.1 |
| | | 5 | 88.2 | 232.6 | 24.4 |
| | | 6 | 89.0 | 229.6 | 24.8 |
| | | 7 | 86.2 | 232.1 | 22.7 |
| AC-W8 | Travel | 1 | 89.1 | 228.3 | 27.3 |
| | | 2 | 96.2 | 231.2 | 20.2 |
| | | 3 | 94.6 | 234.6 | 28.2 |
| | | 4 | 99.3 | 236.4 | 25.5 |
| | | 5 | 90.6 | 233.3 | 26.7 |

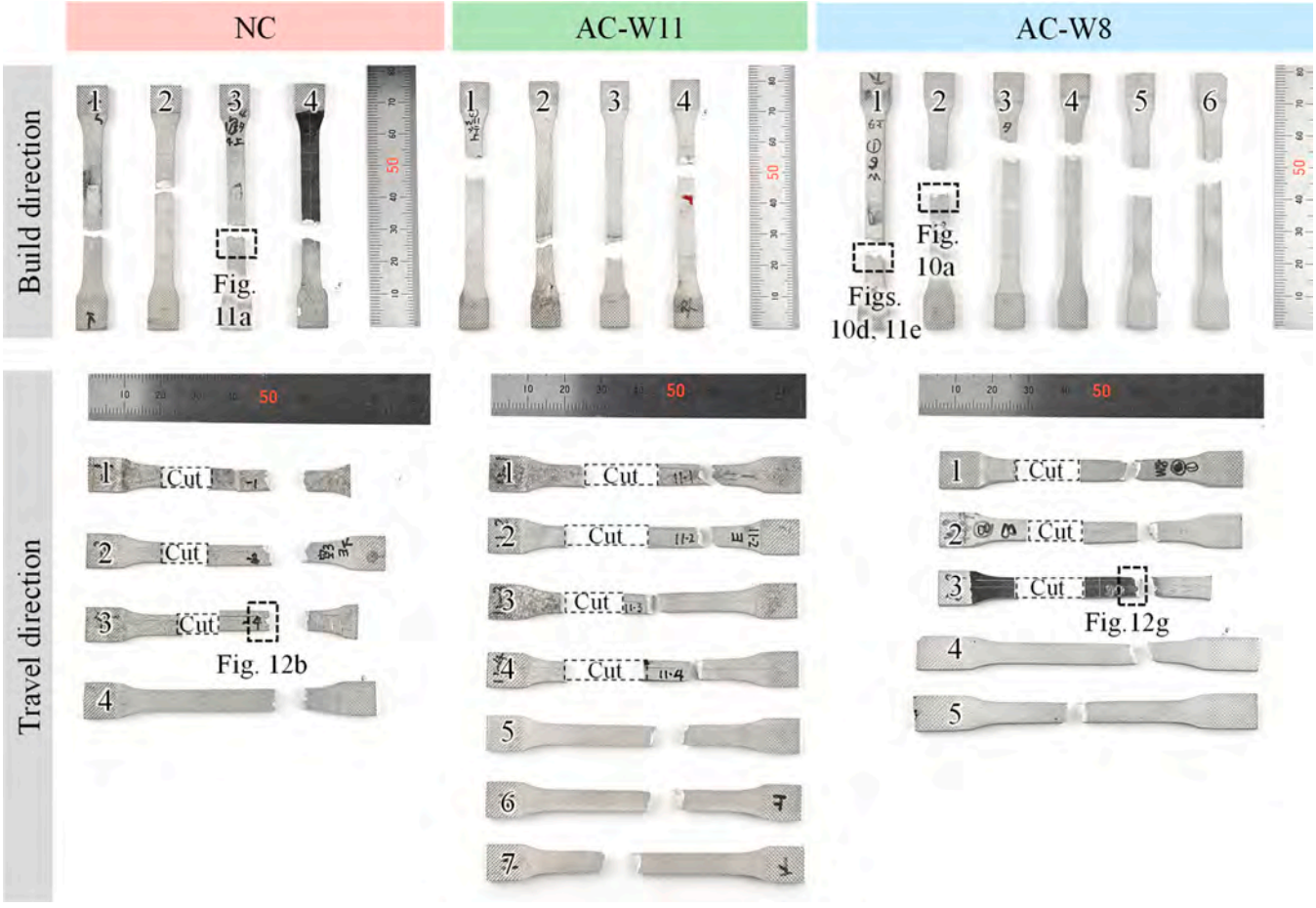


**Fig. A.1.** Macro-scale appearances of all fractured tensile specimens.

## Data availability

The authors confirm that the data supporting the findings of this study are available within the article and/or its supplementary materials.

## References


Al-Kazzaz, H., Medraj, M., Cao, X., Jahazi, M., 2008. Nd:YAG laser welding of aerospace grade ZE41A magnesium alloy: modeling and experimental investigations. Mater. Chem. Phys. 109, 61–76. https://doi.org/10.1016/J.MATCHEMPHYS.2007.10.039.

Casuso, M., Veiga, F., Suárez, A., Bhujangrao, T., Aldalur, E., Artaza, T., Amondarain, J., Lamikiz, A., 2021. Model for the prediction of deformations in the manufacture of thin-walled parts by wire arc additive manufacturing technology. Metals 11, 678. https://doi.org/10.3390/met11050678.

Chapman, J.A., Wilson, D.V., 1962. The room-temperature ductility of fine-grain magnesium. J. Inst. Metals 91, 39–40.

Da Silva, L.J., Souza, D.M., De Araújo, D.B., Reis, R.P., Scotti, A., 2020. Concept and validation of an active cooling technique to mitigate heat accumulation in WAAM. Int. J. Adv. Manuf. Technol. 107, 2513–2523. https://doi.org/10.1007/s00170-020-05201-4.

Goka, S., Manjaiah, M., Davidson, M.J., 2024. Study on mechanical, microstructural and corrosion analysis of wire arc additive manufactured AZ31 magnesium alloy. Met. Mater. Int. https://doi.org/10.1007/s12540-024-01864-w.

Guo, J., Zhou, Y., Liu, C., Wu, Q., Chen, X., Lu, J., 2016. Wire arc additive manufacturing of AZ31 magnesium alloy: grain refinement by adjusting pulse frequency. Materials 9. https://doi.org/10.3390/ma9100823.

Guo, Y., Quan, G., Jiang, Y., Ren, L., Fan, L., Pan, H., 2021. Formability, microstructure evolution and mechanical properties of wire arc additively manufactured AZ80M magnesium alloy using gas tungsten arc welding. J. Magnesium Alloys 9, 192–201. https://doi.org/10.1016/j.jma.2020.01.003.

Hauser, F.E., London, P.R., Dorn, J.E., 1956. Fracture of magnesium alloys at low temperature. JOM 8, 589–592. https://doi.org/10.1007/BF03377735.

Heinrich, L., Feldhausen, T., Saleeby, K., Kurfess, T., Saldaña, C., 2023. Build plate conduction cooling for thermal management of wire arc additive manufactured components. Int. J. Adv. Manuf. Technol. 124, 1557–1567. https://doi.org/10.1007/s00170-022-10558-9.

Huang, K., Marthinsen, K., Zhao, Q., Logé, R.E., 2018. The double-edge effect of second-phase particles on the recrystallization behaviour and associated mechanical properties of metallic materials. Prog. Mater. Sci. 92, 284–359. https://doi.org/10.1016/j.pmatsci.2017.10.004.

Jorge, V.L., Scotti, F.M., Teixeira, F.R., Vilarinho, L.O., Reis, R.P., 2025. Application of near-immersion active cooling for thermal management in arc additive manufacturing of thin super duplex stainless steel walls. Int. J. Adv. Manuf. Technol. 137, 3025–3048. https://doi.org/10.1007/s00170-025-15355-8.

Kamado, S., Tsukuda, M., Tokutomi, I., Hirose, K., 1987. Effect of solidification conditions on mechanical properties of unidirectionally solidified AZ91C alloy. J. Japan Inst. Light Metals 37, 721–728. https://doi.org/10.2464/jilm.37.721.

Kobayashi, T., Koike, J., Yoshida, Y., Kamado, S., Suzuki, M., Maruyama, K., Kojima, Y., 2003. Grain size dependence of active slip systems in an AZ31 magnesium alloy. J. Japan Inst. Metals 67, 149–152. https://doi.org/10.2320/jinstmet1952.67.4_149.

Koike, J., Kobayashi, T., Mukai, T., Watanabe, H., Suzuki, M., Maruyama, K., Higashi, K., 2003. The activity of non-basal slip systems and dynamic recovery at room temperature in fine-grained AZ31B magnesium alloys. Acta Mater. 51, 2055–2065. https://doi.org/10.1016/S1359-6454(03)00005-3.

Ladani, L., Sadeghilaridjani, M., 2021. Review of powder bed fusion additive manufacturing for metals. Metals 11, 1391. https://doi.org/10.3390/met11091391.

Lei, Y., Xiong, J., Li, R., 2018. Effect of inter layer idle time on thermal behavior for multi-layer single-pass thin-walled parts in GMAW-based additive manufacturing. Int. J. Adv. Manuf. Technol. 96, 1355–1365. https://doi.org/10.1007/s00170-018-1699-1.

Li, F., Chen, S., Shi, J., Zhao, Y., Tian, H., 2018. Thermoelectric cooling-aided bead geometry regulation in wire and arc-based additive manufacturing of thin-walled structures. Appl. Sci. 8, 207. https://doi.org/10.3390/app8020207.

Li, K., Li, B., Zhu, L., Hou, X., Li, Z., Murr, L.E., Jiang, B., Pan, F., 2024. Optimizing microstructure and strength of CMT-wire arc additive manufactured WE43 Mg alloy through a novel active cooling technique. Thin-Walled Struct., 112453 https://doi.org/10.1016/j.tws.2024.112453.

Li, X., Zhang, M., Fang, X., Li, Z., Jiao, G., Huang, K., 2023. Improved strength-ductility synergy of directed energy deposited AZ31 magnesium alloy with cryogenic cooling mode. Virtual. Phys. Prototyp. 18, e2170252. https://doi.org/10.1080/17452759.2023.2170252.

Ma, D., Xu, C., Sui, S., Tian, J., Guo, C., Wu, X., Zhang, Z., Shechtman, D., Remennik, S., 2023. Enhanced strength-ductility synergy in a wire and arc additively manufactured Mg alloy via tuning interlayer dwell time. J. Magnes. Alloys 11, 4696–4709. https://doi.org/10.1016/j.jma.2023.01.015.

Ma, P., Wang, C., Jia, H., Yang, Y., Zha, M., 2025. Simultaneous enhancement in deposition efficiency and nano-scale precipitation of high-strength AZ31 Mg alloy via water cooling assisted wire-arc directed energy deposition. Thin-Walled Struct. 206, 112689. https://doi.org/10.1016/j.tws.2024.112689.

Nagamatsu, H., Sasahara, H., 2026. Effect of the active cooling and dwell time to tensile properties of AZ31 wall components by wire-arc directed energy deposition. Int. J. Adv. Manuf. Technol. 144, 1197–1211. https://doi.org/10.1007/s00170-026-17843-x.

Oliveira, J.P., Gouveia, F.M., Santos, T.G., 2022. Micro wire and arc additive manufacturing (μ-WAAM). Addit. Manufact. Lett. 2, 100032. https://doi.org/10.1016/j.addlet.2022.100032.

Rodrigues, T.A., Duarte, V., Miranda, R.M., Santos, T.G., Oliveira, J.P., 2019. Current status and perspectives on wire and arc additive manufacturing (WAAM). Materials 12, 1121. https://doi.org/10.3390/ma12071121.

Savage, W.F., Aronson, A.H., 1966. Preferred orientation in the weld fusion zone. Weld. J. 45, 85s–89s.

Sugiyama, Y., Nakata, J., Miyauchi, H., 1993. Reducing smut in aluminium alloy welds using double wire MIG (DWM) welding. Weld. Int. 7, 177–182. https://doi.org/10.1080/09507119309548369.

Tan, J., Ramakrishna, S., 2021. Applications of magnesium and its alloys: a review. Appl. Sci. 11, 6861. https://doi.org/10.3390/app11156861.

Teixeira, F.R., Scotti, F.M., Jorge, V.L., Scotti, A., 2023. Combined effect of the interlayer temperature with travel speed on features of thin wall WAAM under two cooling approaches. Int. J. Adv. Manuf. Technol. 126, 273–289. https://doi.org/10.1007/s00170-023-11105-w.

Tong, X., Wu, G., Easton, M.A., Sun, M., Wang, Q., Zhang, L., 2023. Microstructural evolution and strengthening mechanism of Mg-Y-RE-Zr alloy fabricated by quasi-directed energy deposition. Addit. Manuf. 67, 103487. https://doi.org/10.1016/j.addma.2023.103487.

Vázquez, L., Rodríguez, N., Rodríguez, I., Alberdi, E., Álvarez, P., 2020. Influence of interpass cooling conditions on microstructure and tensile properties of Ti-6Al-4V parts manufactured by WAAM. Weld. World 64, 1377–1388. https://doi.org/10.1007/s40194-020-00921-3.

WAAM3D Limited, 2021. T-section /made by WAAM at WAAM3D [WWW Document]. https://www.youtube.com/watch?v=CYbF4oFXArM (accessed 6.12.26).

Wang, C., Wang, J., Bento, J., Ding, J., Pardal, G., Chen, G., Qin, J., Suder, W., Williams, S., 2023. A novel cold wire gas metal arc (CW-GMA) process for high productivity additive manufacturing. Addit. Manuf. 73, 103681. https://doi.org/10.1016/j.addma.2023.103681.

Wang, H., Liu, W., Tang, Z., Wang, Y., Mei, X., Saleheen, K.M., Wang, Z., Zhang, H., 2020. Review on adaptive control of laser-directed energy deposition. Opt. Eng. 59, 1. https://doi.org/10.1117/1.OE.59.7.070901.

Wang, P., Zhang, H., Zhu, H., Li, Q., Feng, M., 2021. Wire-arc additive manufacturing of AZ31 magnesium alloy fabricated by cold metal transfer heat source: processing, microstructure, and mechanical behavior. J. Mater. Process. Technol. 288, 116895. https://doi.org/10.1016/j.jmatprotec.2020.116895.

Wang, S., Yan, C., Gu, Z., 2022. Weld formation, microstructure evolution and mechanical property of laser-arc hybrid welded AZ31B magnesium alloy. Metals 12, 696. https://doi.org/10.3390/met12040696.

Xie, Y., Zhang, H., Zhou, F., 2016. Improvement in geometrical accuracy and mechanical property for arc-based additive manufacturing using metamorphic rolling mechanism. J. Manuf. Sci. Eng. 138, 111002. https://doi.org/10.1115/1.4032079.

Yang, W., Yang, H., Yang, K., Wang, X., Hu, C., Lin, X., 2024. Microstructure evolution and mechanical properties of large-size AZ31 magnesium alloy block fabricated by wire arc additive manufacturing. J. Magnes. Alloys. https://doi.org/10.1016/j.jma.2024.04.024. S2213956724001464.

Yang, Y.-H., Guan, Z.-P., Ma, P.-K., Ren, M.-W., Jia, H.-L., Zhao, P., Zha, M., Wang, H.-Y., 2023. Wire arc additive manufacturing of a novel ATZM31 Mg alloy: microstructure evolution and mechanical properties. J. Magnes. Alloys. https://doi.org/10.1016/j.jma.2023.08.014. S2213956723001858.

Yoshida, Y., Arai, K., Itoh, S., Kamado, S., Wada, T., Matsunaga, T., Yoshimoto, T., Kojima, Y., 2005. Effects of Al and Zn contents and heat treatment on microstructures and tensile properties of Mg-Al-Zn alloys. J. Japan Inst. Light Metals 55, 456–462. https://doi.org/10.2464/jilm.55.456.

Yuan, W., Panigrahi, S.K., Su, J.-Q., Mishra, R.S., 2011. Influence of grain size and texture on Hall-Petch relationship for a magnesium alloy. Scr. Mater. 65, 994–997. https://doi.org/10.1016/j.scriptamat.2011.08.028.

Zhao, Y., Jia, Y., Chen, S., Shi, J., Li, F., 2020. Process planning strategy for wire-arc additive manufacturing: thermal behavior considerations. Addit. Manuf. 32, 100935. https://doi.org/10.1016/j.addma.2019.100935.